Molecular Dynamics

International Edition: DOI: 10.1002/anie.201803552
German Edition: DOI: 10.1002/ange.201803552

Real-Time Probing of Nanowire Assembly Kinetics at the Air–Water Interface by In Situ Synchrotron X-Ray Scattering

Zhen He[+], Hui-Jun Jiang[+], Long-Long Wu[+], Jian-Wei Liu, Geng Wang, Xiao Wang, Jin-Long Wang, Zhong-Huai Hou, Gang Chen,* and Shu-Hong Yu**

Abstract: *Although many assembly strategies have been used to successfully construct well-aligned nanowire (NW) assemblies, the understanding of their assembly kinetics has remained elusive, which restricts the development of NW-based device and circuit fabrication. Now a versatile strategy that combines interfacial assembly and synchrotron-based grazing-incidence small-angle X-ray scattering (GISAXS) is presented to track the assembly evolution of the NWs in real time. During the interface assembly process, the randomly dispersed NWs gradually aggregate to form small ordered NW-blocks and finally are constructed into well-defined NW monolayer driven by the conformation entropy. The NW assembly mechanism can be well revealed by the thermodynamic analysis and large-scale molecular dynamics theoretical evaluation. These findings point to new opportunities for understanding NW assembly kinetics and manipulating NW assembled structures by bottom-up strategy.*

Macroscopic-scale nanowire (NW) assemblies with unique structures and designed properties have become one of the most active research areas in chemistry and materials science.[1] In the bottom-up strategies, basic NW building blocks can be hierarchically organized into functional multi-structures, much like the way nature uses proteins to construct complex biological systems and monomer to macromolecules or polymers.[2] However, precisely manipulating and ordering NWs for forming complex NW films still present a major challenge for novel applications,[3] which is restricted by the limited understanding of their assembly mechanisms or assembly kinetics. Electron microscopy techniques were often used as tools to characterize the final structures but failed to probe the in situ intermediate structure owing to their high-vacuum requirement. Compared with electron microscopy techniques, the GISAXS technique has been demonstrated as an efficient technique enabling the real-time tracking of the self-assembly and self-organization process in their working environment.[4] So far, GISAXS is one of the most effective tools for tracking the real-time assembly process of zero-dimensional building blocks.[5] Thermodynamic and kinetic theoretical simulations can be used to effectively predict the nanoparticle assembly behaviors.[4b,6] However, these simulations were always constrained to assembly systems with only a few nanoscale building blocks or on a short time scale.[7] Monte Carlo simulation was introduced to qualitatively investigate the self-assembly process of polyhedral silver nanocrystals into densest packings and superlattices.[7b] Hence, except for a number of special cases, a description that captures the detailed NW interface assembly mechanisms remain elusive.

In this work, we report an in situ characteristic method to investigate in real-time the NW assembly process by combining nanowire interfacial assembly (Langmuir–Blodgett (LB) technique[8] was selected here as a model) and synchrotron-based GISAXS technique which is quantitatively analyzed and further explained in the framework of distorted wave Born approximation (DWBA).[9] Moreover, thermodynamic analysis and kinetic simulation were successfully applied to elucidate the driving forces and mechanisms that guide the NW assembly behavior.

In respect of the uniform size and shapes, Te NWs were selected as a model structural unit.[10] First, Te NWs in mixed solvent of *N*,*N*-dimethylformamide (DMF) and chloroform

[*] Z. He,[+] Dr. J.-W. Liu, Dr. J.-L. Wang, Prof. S.-H. Yu
Division of Nanomaterials & Chemistry, Hefei National Research Center for Physical Sciences at the Microscale, CAS Center for Excellence in Nanoscience, Collaborative Innovation Center of Suzhou Nano Science and Technology, Department of Chemistry Hefei Science Center of CAS, University of Science and Technology of China
Hefei 230026 (China)
E-mail: jwliu13@ustc.edu.cn
shyu@ustc.edu.cn
Dr. H.-J. Jiang,[+] Prof. Z.-H. Hou
Department of Chemical Physics & Hefei National Research Center for Physical Sciences at Microscales, iChEM, University of Science and Technology of China
Hefei 230026 (China)
L.-L. Wu,[+] X. Wang, Prof. G. Chen
School of Physical Science and Technology, ShanghaiTech University
Shanghai 201210 (China),
and
Shanghai Institute of Microsystem and Information Technology, Chinese Academy of Sciences
Shanghai 200050 (China),
and
University of Chinese Academy of Sciences
No.19A Yuquan Road, Beijing 100049 (China)
E-mail: gchen@shanghaitech.edu.cn
Dr. G. Wang
Shanghai Synchrotron Radiation Facility, Shanghai Institute of Applied Physics, Chinese Academy of Sciences
Shanghai 201204 (China)
[+] These authors contributed equally to this work.
Supporting information and the ORCID identification number(s) for the author(s) of this article can be found under: https://doi.org/10.1002/anie.201803552.

were dropped onto the water surface. After the evaporation of mixed solvent, the NWs are floating on the water surface (Figure 1 a), while the immersion depth of the NW is determined by the interfacial energy. The relative interfacial energy of the NW is varied with the NW position with respect to the interface, which can be predicted by Pieranski's model.[11] With the NW gradually surfaces from the water, the interfacial energy experiences a firstly decrease and then increase process (Figure 1 b), while the lowest point at $\tilde{Z} = -0.866$ reveals that nearly 93 % of the NW cross-section are immersed in water (Supporting Information, Method 1).

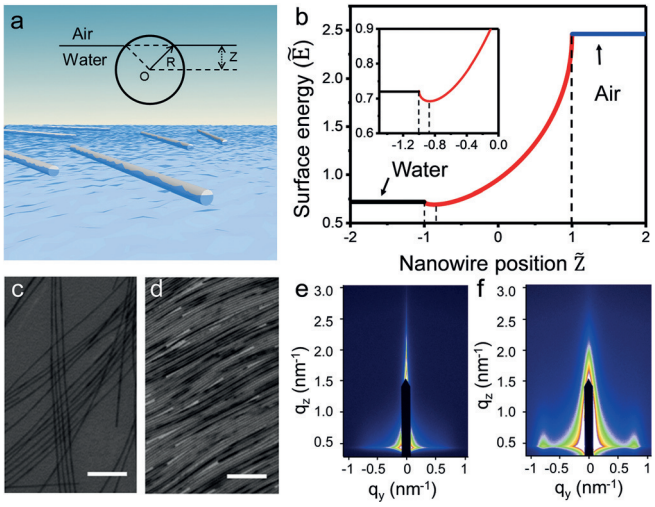

Figure 1. a) Illustration of the NW floating state. Inset: cross-section of a NW (*R* is the NW radius, *Z* is the distance from the center of the NW to the air–water interface). b) Interfacial energy plotted as a function of the NW position with respect to the air–water interface. c),e) Transmission electron microscopy (TEM) image and GISAXS pattern of the disordered NWs before assembly. d),f) TEM image and GISAXS pattern of the ordered NWs after assembly. Scale bars are 500 nm in (c) and (d).

The initial and final states of the NWs are presented in Figure 1 c–f. Initially, Te NWs present a random orientation (Figure 1 c) that shows no scattering peaks in the GISAXS pattern (Figure 1 e). At the end of the assembly process, the obtained Te NW monolayer exhibit a well-aligned structure (Figure 1 d), while two vertical Bragg peaks emerge at $q_y = \pm 0.73$ nm^{-1} (the period of NWs in real space is $2\pi/q_y = 8.6$ nm) in the GISAXS pattern (Figure 1 f).

To investigate the NW assembly process at the air–water interface in real time, we combined interface assembly apparatus (LB trough) with the SAXS platform in the Shanghai Synchrotron Radiation Facility (SSRF; Figure 2 a,b). During the assembling process, the GISAXS scattering signals show continuous changes resulting from the dynamical NW assembly at the air–water interface (Supporting Information, Movie S1). The in situ scattering signal evolution is shown in Figure 2 c, and the intensity evolution of the scattering peak around $q_y = 0.73$ nm^{-1} is highlighted in Figure 2 d. After the NW solution is dropped, the NWs spread and distribute randomly over the LB trough, resulting in small diffuse scattering signals around the central

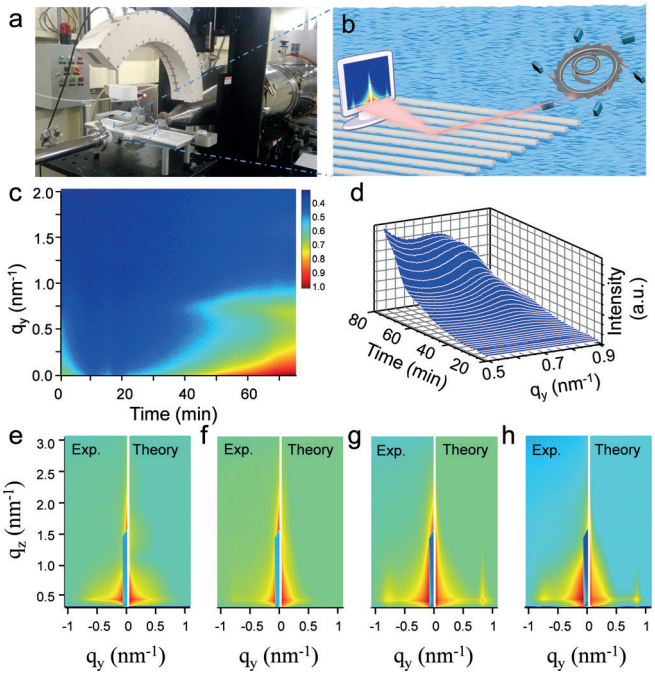

Figure 2. a),b) Photograph and illustration of the experimental setup in the synchrotron facility. c) X-ray scattering intensity evolution extracted from the GISAXS patterns along the q_y direction at $q_z = 0.43$ nm^{-1}. d) The intensity evolution of the scattering peak around at $q_y = 0.73$ nm^{-1}. e)–h) The experimental (left) and simulated (right) GISAXS patterns obtained for NWs at four distinct states: e) randomly dispersed state, f) small blocks composed of aligned NWs, g) well-aligned monolayer state, and h) excessive aligned state.

reflection zone (Figure 2 c and Figure 2 e, left). Because of the larger electron densities of residue solvents than that of water (Supporting Information, Figure S2), these diffuse scattering signals caused by interfacial thermal fluctuations decrease as the evaporation of chloroform and DMF. As shown in Figure 2 e, the experimental GISAXS data (left) are in good agreement with the simulated pattern (right) with the fitting parameters listed in the Supporting Information, Table S1. After 6.5 min of solvent evaporation, it is considered that the Te NWs present a random orientation with large distances. At this very moment, the water surface becomes stable and the diffuse scattering signals become the weakest (Figure 2 c). From 6.5 to 26.5 min during the assembly process, although the barriers start to move, the distance between NWs are still large and there appear no scattering peaks in the GISAXS patterns. From 26.5 to 39 min, as the increased number density of NW, NW blocks appears gradually as well as the diffuse scattering signals around the central zone (Figure 2 c and Figure 2 f, left). The increased intensity attributed to the reduced distance between NWs suggests the increased number of NWs in the same direction. Owing to the confinement of the LB barriers, the orientation of the NW blocks is not completely random but preferably parallel to the barriers.

Employing the DWBA theory (Supporting Information, Method 2), the simulated pattern in Figure 2 f (right) fitted well with the experimental result (left). The corresponding simulated parameters (Supporting Information, Table S2) confirmed that the small blocks on average composed of 11

NWs are formed during this period (Supporting Information, Figure S3a,b).

From 39 to 71 min, with the order of NWs assembly gradually increase, new peaks at $q_y = \pm 0.73\ \mathrm{nm}^{-1}$ emerged with its intensity become stronger (Figures 2c,d). The simulated results together with experimental results confirm these new Bragg peaks (Figure 2g). The intensity of this peak reaches the maximum at the 71st min (Figure 2d; Supporting Information, Figure S4), indicating the formation of well-aligned NW monolayer (Supporting Information, Figure S3c). Upon further compression, the intensity of the Bragg peaks slightly declines (Figure 2h, left), which attribute to the decreased order of NWs assembly. At this state, the well-aligned NW monolayer has been folded in the direction parallel to the LB barriers (Supporting Information, Figure S3d). Besides, the simulated patterns (Figure 2h, right) with the corresponding fitting parameters (Supporting Information, Table S3) agree well with the experimental data (left), which manifest the decreased peak intensity. Furthermore, the black line in the Supporting Information, Figure S5 represents the position of the Yoneda peak for water,[4a,12] which arises at the maximum of the off-specular diffuse scattering intensity. These observations confirm the NWs are trapped in the surface energy minimum and the NW assembling takes place at the air–water interface.

To explain the NW motion behaviors during the assembly process, thermodynamic analysis and corresponding kinetic simulation were employed. A single NW was randomly selected among the whole NW system, while other NWs as well as the barriers of the LB trough were considered as an effective confined boundary. As illustrated in Figure 3a, a NW with the length of L can move randomly in the confined space, and the width of the free path is D (Supporting Information, Method 3).

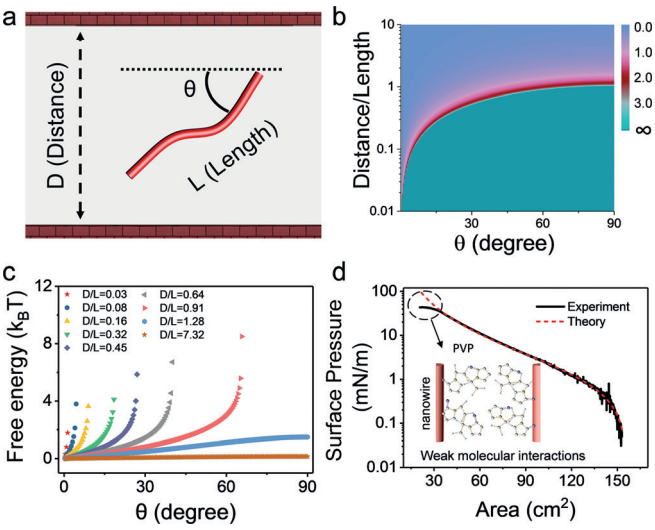

Figure 3. a) The illustration of NW movement in a confined space during the assembly process. b) The color mapping of the free energy distribution of individual NW varied with the D/L ratio and the included angle θ. c) The free energy of individual NW at different D/L ratio varying with the included angle θ. d) The in situ surface pressure (black line) and calculated surface pressure fitting line (red line) as a function of the residual area. Inset: illustration of the weak molecular interactions derived from surfactant of NWs.

In Figure 3b, the free energy encounters the lowest state at high D/L and increase sharply at low D/L. When D is larger than L, for example, $D/L = 7.32$ or 1.28, the free energy of NWs at $\theta = 90$ possess the largest value while $\theta = 0$ occupies the lowest state. As the discrepancy between these two values is smaller than $k_B T$, NWs are hard to assemble. Once the D/L ratio decreases to below 1 (For example, $D/L = 0.91$), an obvious minimum appears at $\theta = 0$, providing an effective driving force for the alignment of NWs. With further decreasing of D/L ratio, the free path of NW movement becomes smaller, and the range of angle allowed for NWs narrows down quickly, resulting in NWs that are forced to align and finally reach a density-aligned state.

It is well-known that the surface pressure is a cognitive factor to influence the assembly process by LB technique. As described in the Supporting Information, Method 3, the surface pressure can be derived theoretically to be proportional to D^{-2}. Several stages of the assembly process can be identified by the comparison between the theoretically predicted (red line) and the experimentally measured (black line) surface pressure in Figure 3d. During the initial stage, the surface pressure keeps at a low level, which means that the distance between NWs is very far from each other, the same with the GISAXS pattern in Figure 2e. As the two barriers of the LB trough get closer, the free space becomes limited gradually, while randomly dispersed NWs tend to form bundles and start to align with each other or the barriers. At this stage, NWs are still separated far away that short-range interactions such as van der Waals forces are very weak and the surface pressure is dominantly contributed by the conformation entropy, which is accordance with the stage discussed in Figure 2f. During these two periods, the experimentally measured line agree well with the theoretical prediction and the assembled NW films are prone to be disassembled and dispersed again when the barriers withdraw (Supporting Information, Movie S2). When the two barriers keep closing, a well-defined NW monolayer can be obtained and the freestanding NW structure remains structurally intact even the barriers withdraw (Supporting Information, Movie S2), which is consistent with the GISAXS pattern in Figure 2g. The capping agent of Te NWs is poly(vinyl pyrrolidone) (PVP) (Figure 3d, inset), which shows a weak molecule interaction when the NW is getting closer. For close-packed NWs, the magnitude of the weak molecule interactions is about 10^3–$10^4\ k_B T$.[13] Thus, the short-range molecule interactions between NWs at this stage are sufficiently strong to obtain a freestanding NW monolayer at the air–water interface. In this stage, the theoretical prediction is higher than the experimentally measured line. Since the theoretical prediction only takes consideration of the factor of entropy, this observation indicates that the attractive potential from the increased weak molecular interactions dominates.

To verify the predicted NW assembly process, we introduce large-scale molecular dynamics to numerically simulate it in a system of M NWs with periodic boundary condition along the y-axis (Supporting Information, Method 4). The NW (ball) is discretized into m beads, which are marked with

coordinates (Figure 4 a). The exclusive volume effect between different NWs as well as that between NWs and the barriers are taken into account. Owing to the thermal noise, NWs move randomly and accidentally collide with each other. The distribution of NW segment angle ω with respect to the y-axis is depicted in Figure 4 b. It is obvious that NWs with a uniform

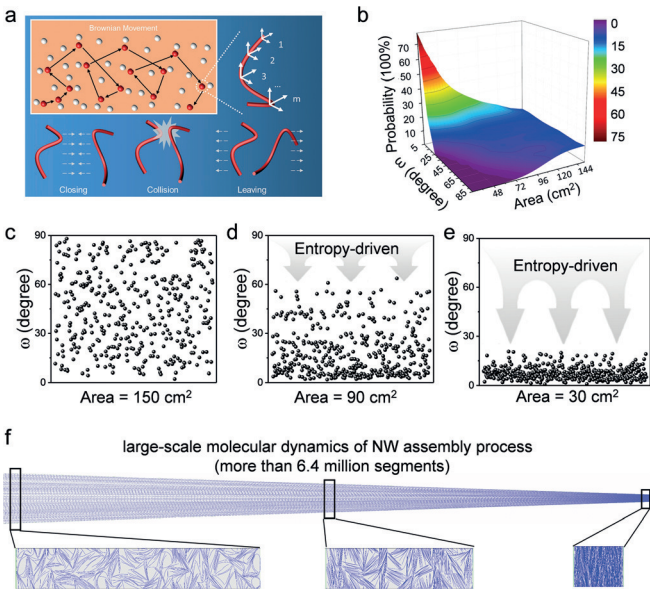

Figure 4. a) Illustration of Brownian movement of NWs on the water surface. b) The 3D plot of the angle distribution of NWs derived from the simulation results during the assembly process. c)–e) The images of the angle distribution of NWs from the simulated results at different stages (residual area of 150, 90, and 30 cm^2, respectively). f) Snapshot of the kinetic simulation based on Brownian dynamics during the assembly process.

distribution state at all the angle scales adjust to accumulate at the low angle state as the two barriers approach each other. The detailed angle distributions in different periods are shown in Figures 4 c–e, where each point represents the angle of an NW segment. In the initial stage, the orientation of NWs is random as well as the axis angle distribution. Then, the number of NWs with larger angles decreases with an accumulation of NWs at the low angle region. Finally, all the NWs locate at low angle region, suggesting a well-aligned structure. Snapshots of the kinetic simulation of NWs is shown in Figure 4 f, from left to right NWs are assembled from a randomly loose state to a final density aligned state. Clearly, local alignment with random directions is formed firstly, and then global alignment emerges when the two barriers are close enough (Supporting Information, Movie S3), which is also in consistent with the experimentally observed dependence of NW ordering on the distance of the barrier.

To demonstrate this versatile strategy to track and guide the NW assembly, the assembly of Te NWs with the diameters of 22 ± 2 nm and 30 ± 2 nm and Ag NWs with a diameter of 55 ± 5 nm were carried out and monitored by in situ GISAXS measurements. As the assembly process evolves, the scattering intensity became obvious gradually, and finally Bragg peaks are at position of $q_y = 0.26\ nm^{-1}$, $0.21\ nm^{-1}$, and $0.11\ nm^{-1}$, respectively, revealing the period of different kinds of NW monolayer (Supporting Information, Figure S6).

In summary, we report an in situ characterization strategy for real-time tracking the evolution of the nanowire assembly. The LB assisted assembly technique was selected here as a model to confirm the validity of the in situ characterization strategy. The in situ assembly process is seen to evolve naturally from the fine details and the mechanism was well revealed by the thermodynamic analysis and large-scale molecular dynamics theoretical evaluation. The results provide insights into the NW interface assembly process and this versatile in situ characterization technique can be applied to investigate various NW interface assembly systems.

Acknowledgements

We acknowledge the funding support from the National Natural Science Foundation of China (Grants 21401183, 21761132008, 21431006, 51471157, 21403204, and 21771168), the Foundation for Innovative Research Groups of the National Natural Science Foundation of China (Grant 21521001), Key Research Program of Frontier Sciences, CAS (Grant QYZDJ-SSW-SLH036), the National Basic Research Program of China (Grant 2014CB931800, 2013CB931800), and the Users with Excellence and Scientific Research Grant of Hefei Science Center of CAS (2015HSC-UE007), the Youth Innovation Promotion Association of CAS (2014298). G.C. acknowledges the supported by NSF of China (11375256, U1632265) and STC of Shanghai Municipality (14JC1493300).

Conflict of interest

The authors declare no conflict of interest.

Keywords: GISAXS · in situ characterization · molecular dynamics simulation · nanowires · thermodynamics simulation

How to cite: *Angew. Chem. Int. Ed.* **2018**, *57*, 8130–8134
Angew. Chem. **2018**, *130*, 8262–8266

[1] a) H. Yan, H. S. Choe, S. W. Nam, Y. J. Hu, S. Das, J. F. Klemic, J. C. Ellenbogen, C. M. Lieber, *Nature* **2011**, *470*, 240–244; b) J.-W. Liu, H.-W. Liang, S.-H. Yu, *Chem. Rev.* **2012**, *112*, 4770–4799; c) J. Lv, K. Hou, D. Ding, D. Wang, B. Han, X. Gao, M. Zhao, L. Shi, J. Guo, Y. Zheng, *Angew. Chem. Int. Ed.* **2017**, *56*, 5055–5060; *Angew. Chem.* **2017**, *129*, 5137–5142.

[2] a) C. Xie, J. Liu, T. M. Fu, X. C. Dai, W. Zhou, C. M. Lieber, *Nat. Mater.* **2015**, *14*, 1286–1292; b) N. A. Kotov, *Science* **2010**, *330*, 188–189; c) C. M. Lieber, *MRS Bull.* **2003**, *28*, 486–491; d) G. Yu, A. Cao, C. M. Lieber, *Nat. Nanotechnol.* **2007**, *2*, 372–377; e) G. Yu, C. M. Lieber, *Pure Appl. Chem.* **2010**, *82*, 2295–2314; f) C. Lu, Z. Tang, *Adv. Mater.* **2016**, *28*, 1096–1108.

[3] a) J. W. Liu, J. L. Wang, Z. H. Wang, W. R. Huang, S. H. Yu, *Angew. Chem. Int. Ed.* **2014**, *53*, 13477–13482; *Angew. Chem.* **2014**, *126*, 13695–13700; b) H. Wu, D. Kong, Z. Ruan, P.-C. Hsu, S. Wang, Z. Yu, T. J. Carney, L. Hu, S. Fan, Y. Cui, *Nat.*

Nanotechnol. **2013**, *8*, 421 – 425; c) P. C. Hsu, D. Kong, S. Wang, H. Wang, A. J. Welch, H. Wu, Y. Cui, *J. Am. Chem. Soc.* **2014**, *136*, 10593 – 10596; d) T. I. Lee, S. Lee, E. Lee, S. Sohn, Y. Lee, S. Lee, G. Moon, D. Kim, Y. S. Kim, J. M. Myoung, Z. L. Wang, *Adv. Mater.* **2013**, *25*, 2920 – 2925; e) M. Li, R. B. Bhiladvala, T. J. Morrow, J. A. Sioss, K.-K. Lew, J. M. Redwing, C. D. Keating, T. S. Mayer, *Nat. Nanotechnol.* **2008**, *3*, 88 – 92; f) J. W. Oh, W. J. Chung, K. Heo, H. E. Jin, B. Y. Lee, E. Wang, C. Zueger, W. Wong, J. Meyer, C. Kim, S. Y. Lee, W. G. Kim, M. Zemla, M. Auer, A. Hexemer, S. W. Lee, *Nat. Commun.* **2014**, *5*, 3043; g) Y. Kim, J. Zhu, B. Yeom, M. Di Prima, X. Su, J. G. Kim, S. J. Yoo, C. Uher, N. A. Kotov, *Nature* **2013**, *500*, 59 – 63.

[4] a) T. Li, A. J. Senesi, B. Lee, *Chem. Rev.* **2016**, *116*, 11128 – 11180; b) J. Gong, R. S. Newman, M. Engel, M. Zhao, F. Bian, S. C. Glotzer, Z. Tang, *Nat. Commun.* **2017**, *8*, 14038; c) F. Lin, Y. Liu, X. Yu, L. Cheng, A. Singer, O. G. Shpyrko, H. L. Xin, N. Tamura, C. Tian, T. C. Weng, X. Q. Yang, Y. S. Meng, D. Nordlund, W. Yang, M. M. Doeff, *Chem. Rev.* **2017**, *117*, 113123 – 113186; d) S. P. Meisburger, W. C. Thomas, M. B. Watkins, N. Ando, *Chem. Rev.* **2017**, *117*, 7615 – 7672; e) Y. Sun, X. Zuo, S. K. R. S. Sankaranarayanan, S. Peng, B. Narayanan, G. Kamath, *Science* **2017**, *356*, 303 – 307; f) L. Wu, J. J. Willis, I. S. McKay, B. T. Diroll, J. Qin, M. Cargnello, C. J. Tassone, *Nature* **2017**, *548*, 197 – 201.

[5] a) J. J. Geuchies, C. van Overbeek, W. H. Evers, B. Goris, A. de Backer, A. P. Gantapara, F. T. Rabouw, J. Hilhorst, J. L. Peters, O. Konovalov, A. V. Petukhov, M. Dijkstra, L. D. Siebbeles, S. van Aert, S. Bals, D. Vanmaekelbergh, *Nat. Mater.* **2016**, *15*, 1248 – 1254; b) L. Ji, G. N. Guo, H. Y. Sheng, S. L. Qin, B. W. Wang, D. D. Han, T. T. Li, D. Yang, A. G. Dong, *Chem. Mater.* **2016**, *28*, 3823 – 3830; c) M. C. Weidman, D. M. Smilgies, W. A. Tisdale, *Nat. Mater.* **2016**, *15*, 775 – 781; d) M. Agthe, T. S. Plivelic, A. Labrador, L. Bergström, G. Salazar-Alvarez, *Nano Lett.* **2016**, *16*, 6838 – 6843.

[6] a) Y. Xia, T. D. Nguyen, M. Yang, B. Lee, A. Santos, P. Podsiadlo, Z. Tang, S. C. Glotzer, N. A. Kotov, *Nat. Nanotechnol.* **2011**, *6*, 580 – 587; b) L. Shi, L. Zhu, J. Guo, L. Zhang, Y. Shi, Y. Zhang, K. Hou, Y. Zheng, Y. Zhu, J. Lv, *Angew. Chem. Int. Ed.* **2017**, *56*, 15397 – 15401; *Angew. Chem.* **2017**, *129*, 15599 – 15603.

[7] a) P. F. Damasceno, M. Engel, S. C. Glotzer, *Science* **2012**, *337*, 453 – 457; b) J. Henzie, M. Grunwald, A. Widmer-Cooper, P. L. Geissler, P. D. Yang, *Nat. Mater.* **2012**, *11*, 131 – 137; c) T. Wang, J. Zhuang, J. Lynch, O. Chen, Z. Wang, X. Wang, D. LaMontagne, H. Wu, Z. Wang, Y. C. Cao, *Science* **2012**, *338*, 358 – 363.

[8] a) S. Paul, C. Pearson, A. Molloy, M. A. Cousins, M. Green, S. Kolliopoulou, P. Dimitrakis, P. Normand, D. Tsoukalas, M. C. Petty, *Nano Lett.* **2003**, *3*, 533 – 536; b) D. Whang, S. Jin, Y. Wu, C. M. Lieber, *Nano Lett.* **2003**, *3*, 1255 – 1259; c) P. Yang, *Nature* **2003**, *425*, 243 – 244; d) S. Acharya, A. B. Panda, N. Belman, S. Efrima, Y. Golan, *Adv. Mater.* **2006**, *18*, 210 – 213; e) A. R. Tao, J. Huang, P. Yang, *Acc. Chem. Res.* **2008**, *41*, 1662 – 1673.

[9] a) N. Hansen, A. Ostermeier, *Evol. Comput.* **2001**, *9*, 159 – 195; b) L. Wu, Y. Liu, X. Wang, G. Wang, D. Zhao, G. Chen, *Appl. Phys. Lett.* **2017**, *110*, 041603.

[10] a) J. Xu, S. Xin, J.-W. Liu, J.-L. Wang, Y. Lei, S.-H. Yu, *Adv. Funct. Mater.* **2016**, *26*, 3580 – 3588; b) B. C. Yang, B. S. Wan, Q. H. Zhou, Y. Wang, W. T. Hu, W. M. Lv, Q. Chen, Z. M. Zeng, F. S. Wen, J. Y. Xiang, S. J. Yuan, J. L. Wang, B. S. Zhang, W. H. Wang, J. Y. Zhang, B. Xu, Z. S. Zhao, Y. J. Tian, Z. Y. Liu, *Adv. Mater.* **2016**, *28*, 9408 – 9415; c) Z. He, Y. Yang, J.-W. Liu, S.-H. Yu, *Chem. Soc. Rev.* **2017**, *46*, 2732 – 2753.

[11] a) T. Li, G. Brandani, D. Marenduzzo, P. Clegg, *Phys. Rev. Lett.* **2017**, *119*, 018001; b) P. Pieranski, *Phys. Rev. Lett.* **1980**, *45*, 569 – 572.

[12] F. Lu, K. G. Yager, Y. Zhang, H. Xin, O. Gang, *Nat. Commun.* **2015**, *6*, 6912.

[13] Z. Zhang, Y. Fu, W. Yu, X. Y. Qin, Z. J. Xue, Y. Liu, D. Luo, C. Yan, X. H. Sun, T. Wang, *Adv. Mater.* **2016**, *28*, 9589 – 9595.

Manuscript received: March 24, 2018
Accepted manuscript online: May 11, 2018
Version of record online: June 6, 2018

